Research Square

Preprints are preliminary reports that have not undergone peer review. They should not be considered conclusive, used to inform clinical practice, or referenced by the media as validated information.

A moon-sized, highly magnetised and rapidly rotating white dwarf may be headed toward collapse

Ilaria Caiazzo (ilariac@caltech.edu)
Caltech https://orcid.org/0000-0002-4770-5388

Kevin Burdge
California Institute of Technology https://orcid.org/0000-0002-7226-836X

James Fuller
Caltech https://orcid.org/0000-0002-4544-0750

Jeremy Heyl
University of British Columbia https://orcid.org/0000-0001-9739-367X

Shri Kulkarni
Caltech Optical Observatories

Thomas Prince
Division of Physics, Mathematics, and Astronomy, California Institute of Technology, Pasadena, CA 91125 https://orcid.org/0000-0002-8850-3627

Harvey Richer
University of British Columbia

Josiah Schwab
UCSC

Igor Andreoni
Caltech

Andrew Drake
California Institute of Technology

Dmitry Duev
California Institute of Technology https://orcid.org/0000-0001-5060-8733

George Helou
Caltech https://orcid.org/0000-0003-3367-3415

Ashish Mahabal
Caltech https://orcid.org/0000-0003-2242-0244

Frank Masci
Caltech https://orcid.org/0000-0002-8532-9395

Roger Smith
California Institute of Technology

Maayane Soumagnac
Weizmann Institute of Science

Physical Sciences - Article

Keywords: Dynamo, Chandrasekhar Mass, Electron Capture, Thermonuclear Supernova, Neutron Stars

Posted Date: November 9th, 2020

DOI: https://doi.org/10.21203/rs.3.rs-99143/v1

License: This work is licensed under a Creative Commons Attribution 4.0 International License.
Read Full License

Version of Record: A version of this preprint was published at Nature on June 30th, 2021. See the published version at https://doi.org/10.1038/s41586-021-03615-y.

A moon-sized, highly magnetised and rapidly rotating white dwarf may be headed toward collapse

Ilaria Caiazzo*†[1], Kevin B. Burdge[1], James Fuller[1], Jeremy Heyl[2], S. R. Kulkarni[1], Thomas A. Prince[1], Harvey Richer[2], Josiah Schwab[3], Igor Andreoni[1], Andrew Drake[1], Dmitry A. Duev[1], George Helou[4], Ashish A. Mahabal[1,5] Frank J. Masci[4], Roger Smith[6], Maayane T. Soumagnac[7,8]

[1]*Division of Physics, Mathematics and Astronomy, California Institute of Technology, Pasadena, CA 91125, USA*

[2]*Department of Physics and Astronomy, University of British Columbia, Vancouver, BC, V6T1Z1, Canada*

[3]*Department of Astronomy and Astrophysics, University of California, Santa Cruz, CA 95064, USA*

[4]*IPAC, California Institute of Technology, 1200 E. California Blvd, Pasadena, CA 91125, USA*

[5]*Center for Data Driven Discovery, California Institute of Technology, Pasadena, CA 91125, USA*

[6]*Caltech Optical Observatories, California Institute of Technology, Pasadena, CA 91125, USA*

[7]*Lawrence Berkeley National Laboratory, 1 Cyclotron Road, Berkeley, CA 94720, USA*

[8]*Department of Particle Physics and Astrophysics, Weizmann Institute of Science, Rehovot 76100, Israel*

White dwarfs represent the last stage of evolution for low and intermediate-mass stars (below about 8 times the mass of our Sun), and like their stellar progenitors, they are often found

*email: ilariac@caltech.edu
†Sherman Fairchild Fellow

in binaries[1–3]. If the orbital period of the binary is short enough, energy losses from gravitational wave radiation can shrink the orbit until the two white dwarfs come into contact and merge[4]. Depending on the masses of the coalescing white dwarfs, the merger can lead to a supernova of type Ia, or it can give birth to a massive white dwarf[5]. In the latter case, the white dwarf remnant is expected to be highly magnetised[6,7] due to the strong dynamo that may arise during the merger, and rapidly rotating due to conservation of the orbital angular momentum of the binary[8]. Here we report the discovery of a white dwarf, ZTF J190132.9+145808.7, which presents all these properties, but to an extreme: a rotation period of 6.94 minutes, one of the shortest measured for an isolated white dwarf[9,10], a magnetic field ranging between 600 MG and 900 MG over its surface, one of the highest fields ever detected on a white dwarf[11], and a stellar radius of 1810 km, slightly larger than the radius of the Moon. Such a small radius implies the star's mass is the closest ever detected to the white dwarf maximum mass, or Chandrasekhar mass[12]. In fact, as the white dwarf cools and its composition stratifies, it may become unstable and collapse due to electron capture, exploding into a thermonuclear supernova or collapsing into a neutron star. Neutron stars born in this fashion could account for $\sim$10% of their total population.

The Zwicky Transient Facility[13–15] (ZTF) is a synoptic optical survey that uses the 48-inch Samuel Oschin Telescope of the Palomar Observatory to image the Northern sky on a regular basis. We discovered ZTF J190132.9+145808.7 (hereafter ZTF J1901+1458) during a search for fast variability in massive white dwarfs. To this end, we selected objects in a white dwarf catalogue[16] that lie below the main white dwarf cooling sequence in the Gaia[17] color-magnitude diagram (CMD,

see Fig. 1). ZTF J1901+1458 showed a small photometric variation with a very short period. With the high-speed imaging photometer *CHIMERA*[18] on the 200-inch Hale telescope, we confirmed a period of 6.94 minutes and a photometric variation amplitude of about 3% (Fig. 2). The period of ZTF J1901+1458 is unusually short for a white dwarf, as typical white dwarf rotational periods are in the range of hours to days[19–21]. The period and ephemeris are listed in Table 1, where T_0 in each filter corresponds to a minimum in the lightcurve.

In order to identify the spectral type of the white dwarf and the origin of its variability, we obtained phase-resolved spectra using the Low Resolution Imaging Spectrometer (*LRIS*)[27] on the 10-m W. M. Keck I Telescope on Mauna Kea. The phase-averaged spectrum is shown in the upper panels of Fig. 3. The spectrum presents broad and shallow features that we identify as hydrogen absorption lines in a high magnetic field. The presence of a strong magnetic field lifts the degeneracies in the electron energy levels of the hydrogen atom. As a result, the zero-field transitions are split and shifted in energy by a value that depends on the strength of the field. To this end, we considered all the allowed bound-bound hydrogen transitions, tabulated in[28]. The wavelengths of the strongest transitions as a function of magnetic field strength are shown in the lower panels of Fig. 3, and the identified spectral lines are listed in Extended Data Table 2.

We find that most of the spectral features are well characterised by a field strength of about 800 million Gauss (MG, red horizontal line), one of the highest fields ever detected on a white dwarf[11]. As the absorption features indicate the average field strength over the surface, the field at the magnetic pole is bound to be higher. By analysing the phase-resolved spectra (Extended Data

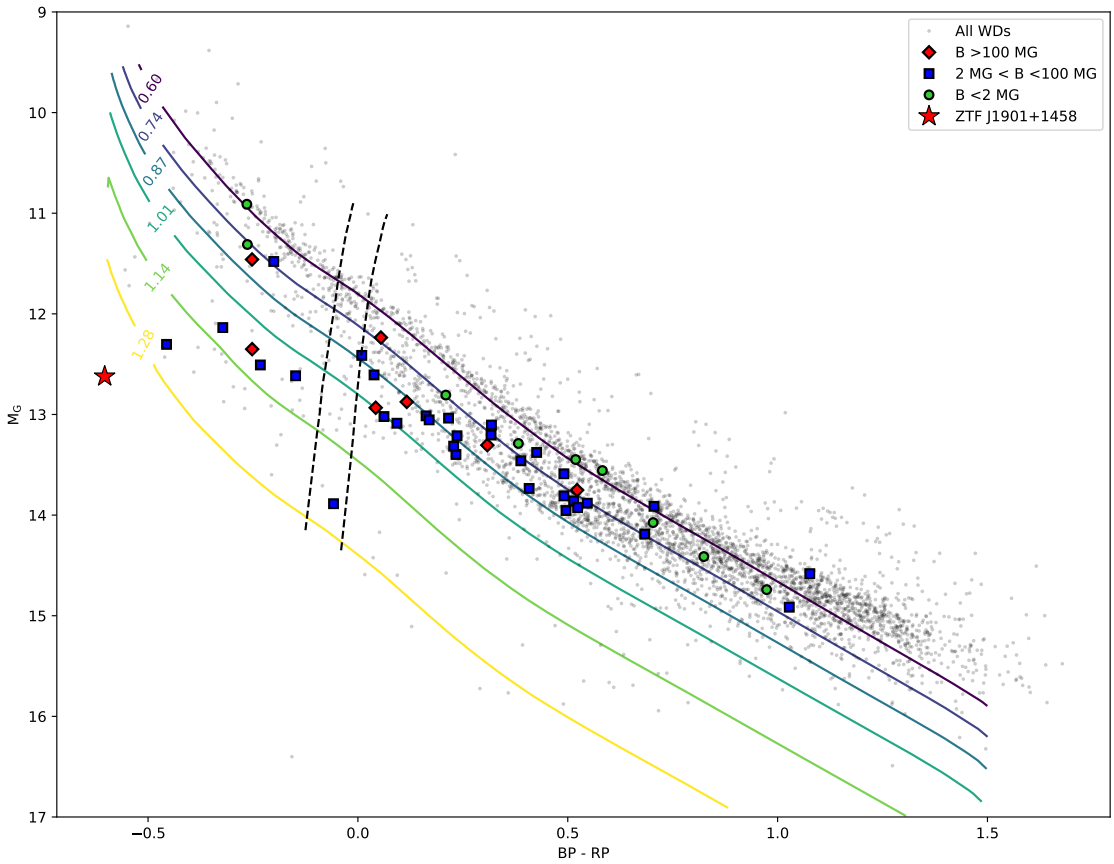

Figure 1: **Gaia CMD.** Gaia color-magnitude diagram for the white dwarfs that are within 100 pc from Earth and within the SDSS footprint[22]. Solid lines show theoretical cooling tracks for white dwarfs with masses between 0.6 $M_\odot$ (top) and 1.28 $M_\odot$ (bottom), equally spaced in mass; the atmosphere is assumed to be hydrogen-dominated[23] and the interior composition to be carbon-oxygen[24] for $M < 1.1$ $M_\odot$ and oxygen-neon[25] for $M > 1.1$ $M_\odot$. Coloured markers indicate white dwarfs for which a magnetic field was measured[11]. ZTF J1901+1458 is shown as a red star, and its location in the CMD reveals its high mass. Vertical dashed lines indicate the location of the ZZ-Ceti instability strip[26]. While ZTF J1901+1458's period is consistent with what is expected for non-radial pulsations, its temperature places it far away from the instability strip. Reddening corrections were applied only to ZTF J1901+1458; as the objects in the sample are close, reddening is expected to be small.

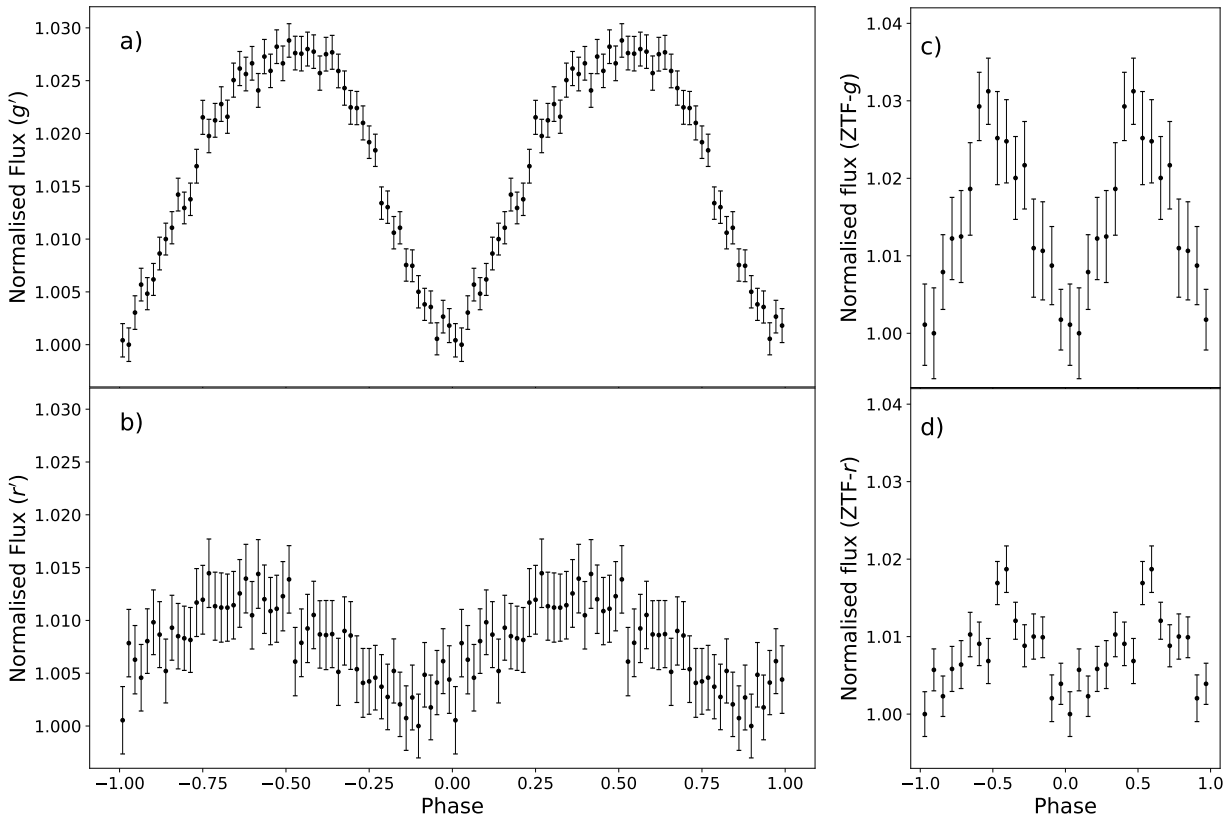

Figure 2: **ZTF J1901+1458 lightcurve** The left panels show the binned CHIMERA lightcurve phase-folded at a period of 6.94 minutes in the g'-band (**a**) and in the r'-band (**b**). The flux has been normalised to the minimum of the lightcurve in each band. The amplitude of the photometric variation is higher in the g'-band (about 3% peak-to-peak) than in the r'-band ($\sim 1.5\%$). Additionally, the two filters show a difference in phase: the red lags the green by about 51 s. The right panels show the similarly normalised ZTF discovery lightcurve in the ZTF g-band (**c**) and $r-$band (**d**). The error bars indicate 1-σ errors.

Fig. 7 and 8), one notices that some of the features become narrower or broader depending on the phase, and the feature at ~ 4600 Å shifts in wavelength, which is why the co-added spectrum shows an additional dip at ~ 4500 Å. This also indicates that in some regions of the white dwarf's surface the magnetic field is as low as 600 MG. The likely explanation for the photometric variation, confirmed by the variations of absorption features with phase, is thus the combination of magnetic dichroism and rotation: the high magnetic field causes variations in the continuum opacities and therefore, as the star rotates, we detect changes in flux as a function of the field strength across the stellar surface. Depending on the strength and structure of the magnetic field, magnetic dichroism can account for a 10% photometric variation[29], and therefore it can easily explain the 3% amplitude observed in ZTF J1901+1458.

To determine the temperature and radius of the white dwarf, we obtained photometric measurements in the near UV using the UVOT (Ultraviolet/Optical Telescope) instrument[30] on the Neil Gehrels Swift Observatory[31]. For optical photometric data we used the Pan-STARRS Survey[32] (PS1). By fitting the photometry, we found the effective temperature and stellar radius of the white dwarf to be $T_{\rm eff} = 80,450^{+330}_{-450}$ K and $R_* = 1,809^{+15}_{-11}$ km, respectively. We also considered the interstellar reddening as a free parameter, and found $E(B-V) = 0.076^{+0.003}_{-0.005}$ (see the Methods section). The white dwarf's radius, whose precise estimate was possible thanks to Gaia's exquisite measurement of the white dwarf's parallax, is slightly larger than the radius of the Moon and is the smallest ever measured for a white dwarf. This also implies that the white dwarf is possibly the most massive ever discovered.

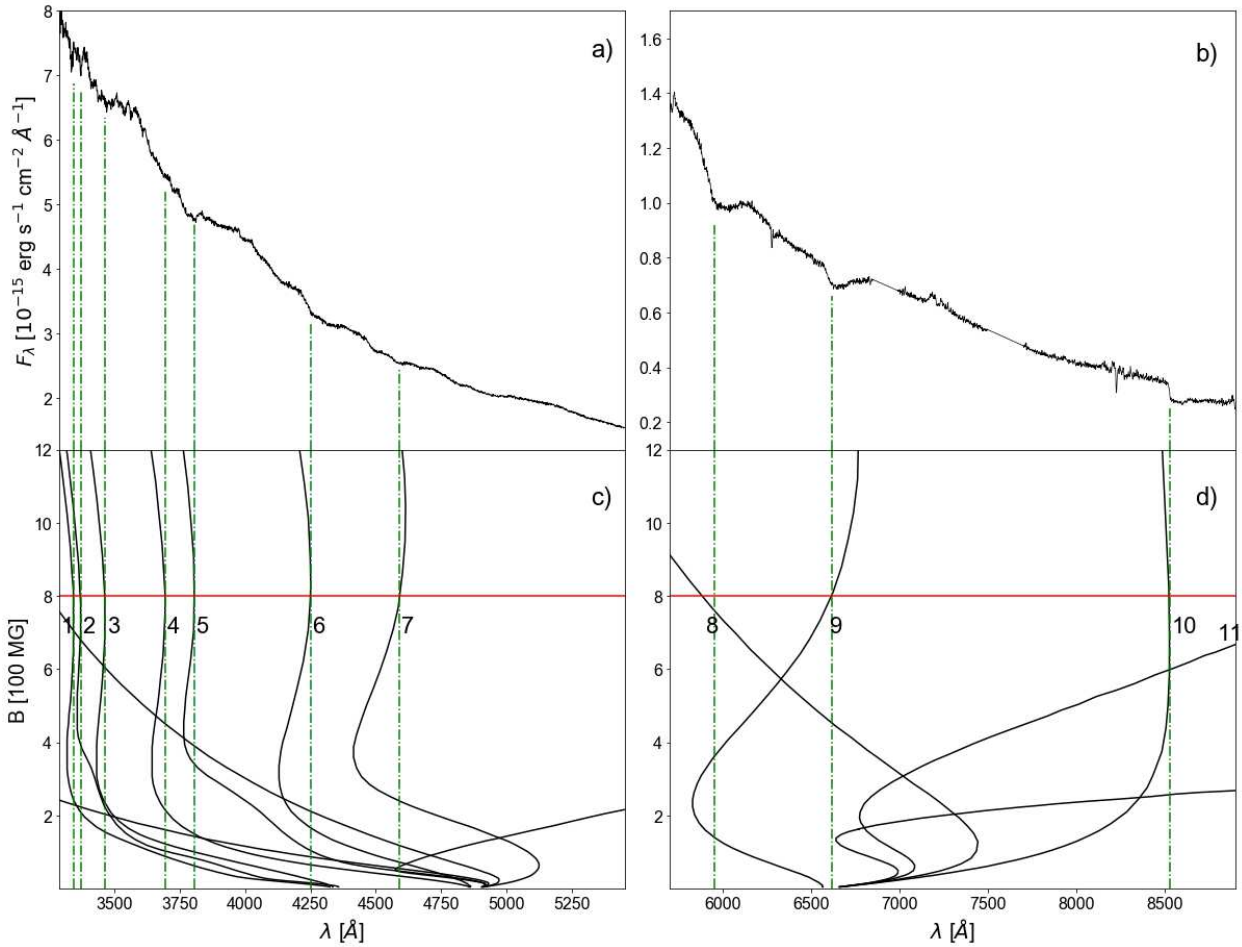

Figure 3: **ZTF J1901+1458 optical spectrum.** The LRIS phase-averaged spectrum of ZTF J1901+1458 is shown in black in the upper panels for the blue (**a**) and red (**b**) sections. In (**c**)-(**d**) the spectrum is compared to predicted line positions of Hα, Hβ and Hγ as a function of magnetic field[28], showing that the white dwarf is characterised by a field strength of about 800 MG (red horizontal solid line). The identified absorption features are highlighted by the green dash-and-dotted lines and numbered, and the respective transitions are listed in Extended Data Table 2.

The mass of the white dwarf can be determined, assuming a composition for its interior, from a mass-radius relation (Fig. 4). At a mass above ~ 1.1 $M_\odot$, the core composition of a white dwarf born from a single-star evolution is expected to be mostly oxygen and neon, with traces of carbon, sodium and magnesium[25,33,34]. Even in the case of formation due to a white-dwarf merger, compressional heating due to rapid accretion is expected to ignite off-center carbon burning[35–37]. This will transform the remnant into a O/Ne white dwarf[8]. Depending on the internal composition, the white dwarf has a mass between 1.350 and 1.371 solar masses.

Two other extremely massive white dwarfs for which a radius has been measured are RE J0317-853[38] and WD1832+089[10], both with a radius of about 2,500 km. Quite curiously, they are both variable with short periods (6 and 12 minutes respectively), and while WD1832+089 does not show indications of a magnetic field, RE J0317-853 is also strongly magnetised, with a field that varies between 185 and 425 MG over its surface[29]. It is likely that both ZTF J1901+1458 and RE J0317-853 are extremely massive, magnetic and rapidly rotating because they are remnants of a white dwarf merger, but while RE J0317-853 is stable and will cool as a white dwarf forever, ZTF J1901+1458 may suffer a very different fate.

At the very high densities reached in the centre of ZTF J1901+1458, the nuclei of some elements undergo electron capture (also called inverse beta-decay). If, for instance, the beta-decay threshold density for sodium is reached at some radius within the star, all the sodium atoms at smaller radii would capture an electron and convert into neon, removing the same electrons that contribute to the degeneracy pressure that keeps the star from collapsing. The effect is to lower

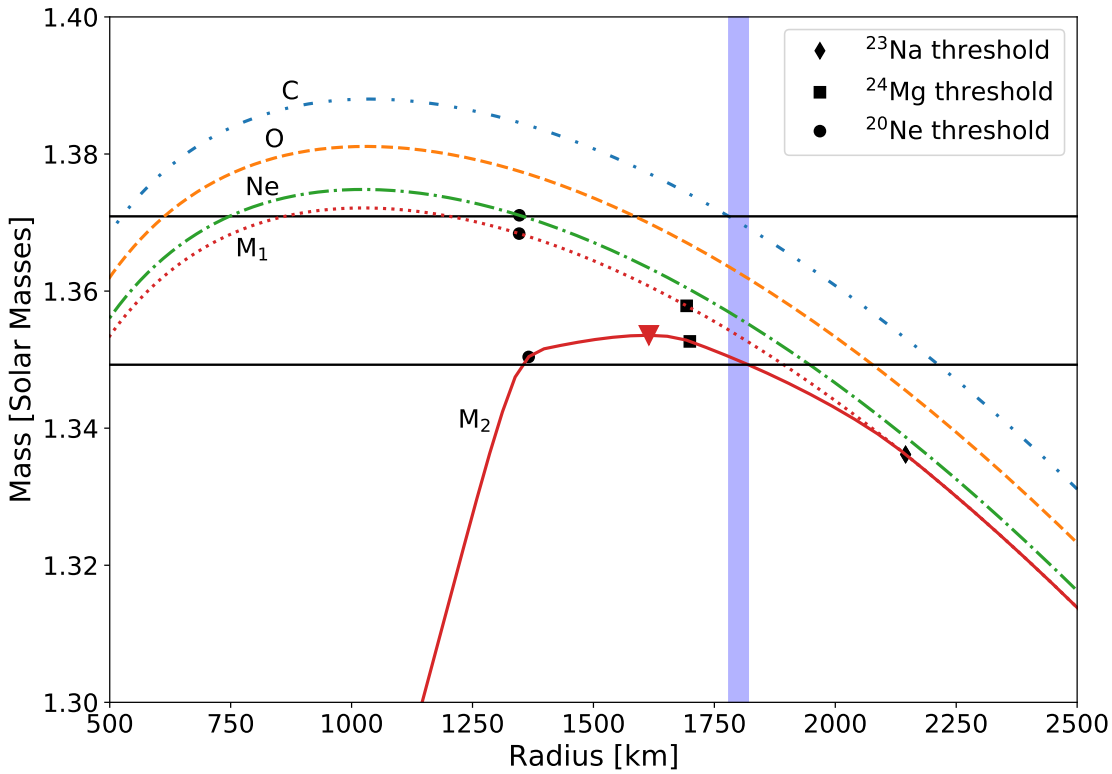

Figure 4: **Mass-radius relation.** The white dwarf mass-radius relation at the temperature of ZTF J1901+1458 (∼80,000 K) is shown for different compositions neglecting the effect of electron captures: carbon C; oxygen O; neon Ne; and the mixture that is thought to result from carbon burning (M_1), specifically 58% oxygen, 30% neon, 2% carbon, 5% sodium, and 5% magnesium[25]. The lowermost red solid curve (M_2) traces the result from the carbon-burning-ash mixture including the effect of electron captures (see text). The black dots along each track indicate the central density threshold for inverse beta-decay of neon (circle), magnesium (square) and sodium (diamond). The vertical blue-shaded area indicates the observed radius of ZTF J1901+1458 within 1-σ errors. A red triangle indicates the maximum mass of 1.354 $M_\odot$ at a radius of 1,600 km along the track of the mixed composition. The horizontal black solid lines highlight the mass determined using a radius of 1798 km for the upper line (pure C), 1.371 $M_\odot$ and of 1824 km for the lower line (carbon-burning-ash mixture), 1.350 $M_\odot$,.

the maximum mass that can be sustained against gravity, and to reduce the equilibrium radius for a fixed mass (see Fig. 4, solid red curve). When the threshold density is reached for magnesium, the effect is even stronger as magnesium undergoes double beta-decay: a ^{24}Mg nucleus captures two electrons and converts into a ^{24}Ne nucleus. If ZTF J1901+1458 has, as is expected from its mass, an oxygen-neon internal composition, its central density is above the threshold for electron capture on sodium and its mass is within one percent of the highest possible mass for a white dwarf.

Inverse beta-decay produces neutrinos, which escape and carry away energy, contributing to the cooling of the white dwarf. Assuming a thermal structure consistent with the luminosity of the white dwarf[39], we estimate the temperature in the core to be about 7×10^7 K. At such a high central temperature and density, ZTF J1901+1458 is the first white dwarf discovered to be cooling mainly through the Urca process on ^{23}Na [40,41]. This unusual neutrino cooling makes an age determination difficult, and further studies are necessary to estimate the age with precision. Using a 1.29 $M_\odot$ model[25] as a reference, we estimate the age of ZTF J1901+1458 to be < 10 Myr.

The mass-radius relation in Fig. 4 was calculated assuming that the core is fully mixed and the composition in the core is homogeneous. Since ZTF J1901+1458 is less than 10 Myr old, this is a good assumption, but over the next few hundred million years, the heaviest elements, including sodium, will gradually sink to the centre[42]. Much of the remaining ^{23}Na will therefore undergo beta-decay, reducing the number of electrons in the star and its radius. The only thing that can stop this process is if the core crystallises before enough sodium can reach the centre, as crystallisation would de facto freeze the composition gradient. If at least sixty percent of the ^{23}Na manages to sink

and decay before the core crystallises, electron-capture on ^{24}Mg will ensue and the radius of the white dwarf will shrink to about 1,550 km. The central density at this point will be 6×10^9 g cm^{-3}, still below the threshold for electron capture on neon, but the mass of the white dwarf will be above the maximum mass (the red triangle in Fig. 4 will have sunk below the lower black horizontal line). The internal pressure will be insufficient to support the star, and the star will begin to collapse, heat up and start electron capture onto neon and nuclear burning of oxygen. Depending on the details of the oxygen burning, the white dwarf will either explode to create a thermonuclear supernova or implode to form a neutron star[41,43,44].

The meta-stable state of ZTF J1901+1458 depends on the timescales for sedimentation, electron capture, and core crystallisation, which are all quite uncertain for such an object. However, the possibility of collapse is intriguing as it would imply a new formation channel for neutron stars, different from the usual core-collapse supernova or the still debated accretion-induced collapse of a white dwarf. If we assume angular momentum and flux conservation, both the spin rate and magnetic field will be amplified by a factor $\sim 2 \times 10^4$ during collapse, and therefore, we expect the newly born neutron star to be similar to a young pulsar, with a magnetic field of $\sim 2 \times 10^{13}$ G, and a spin period of $\sim$ 20 ms. In contrast to regular neutron stars born in core-collapse supernovae, a neutron star born in an electron-capture-induced collapse would not receive a strong kick. We would therefore expect such a neutron star population to be more concentrated in the Galactic plane. Having found ZTF J1901+1458 at only 41 parsecs from Earth means that this type of object cannot be very rare. If we assume a typical distance of ~ 50 pc within which we could detect such a white dwarf within its lifetime of a few hundred million years, the rate of neutron stars born

through white dwarf collapse in the Galaxy would be $\sim 3 \times 10^{-3}$ per year, which is a significant fraction compared to the core-collapse supernova rate of $\sim 2 \times 10^{-2}$ per year[45,46].

Table 1: ZTF J1901+1458 parameters. The ephemeris T_0, in Barycentric Modified Julian Date, corresponds to a minimum in the light curve and it is given separately for the ZTF g-band and r-band because the latter lags behind the former by 51 seconds.

Gaia ID	Parallax [mas]	$\mu_{\rm RA}$ [mas]	$\mu_{\rm DEC}$ [mas]
4506869128279648512	24.13 ± 0.06	95.50 ± 0.09	72.45 ± 0.09
$T_{\rm eff}$ [K]	R_* [km]	M [$\rm M_\odot$]	$E(B-V)$
$80,450^{+330}_{-450}$	$1,809^{+15}_{-11}$	$1.350 - 1.371$	$0.076^{+0.003}_{-0.005}$
T_0 (g) [$\rm BMJD_{TDB}$]	T_0 (r) [$\rm BMJD_{TDB}$]	P [s]	$\dot{P}$ [s s^{-1}]
$59079.217290 \pm 0.000012$	59079.21670 ± 0.00006	416.2427 ± 0.0002	$< 10^{-11}$

Methods

Period Detection Our search for periodicity in massive white dwarfs was part of a broader search for periodic variability on and around the white dwarf cooling track with ZTF, which has already yielded several results, including finding numerous double white dwarf binaries[2,3,47]. The targets were selected using Pan-STARRS (PS1) source catalogue[32], after imposing a photometric colour selection of $(g-r) < 0.2$ and $(r-i) < 0.2$. As the sensitivity of period finding depends strongly on the number of samples in the lightcurve, we limited the search to those targets for which 50 or more photometric 5σ detections are available in the ZTF archival data. In order to maximise the number of epochs for each lightcurve, we combined data from multiple filters by computing the median magnitude in each filter, and shifting g- and i-band so that their median magnitude matched the r-band data. We used a graphics processing unit (GPU) implementation of the conditional entropy period finding algorithm[48]. We cross-matched our candidates with the Gaia DR2 catalogue[49] and visually inspected the lightcurves of those objects that lie below the main white dwarf cooling track in the Gaia CMD. ZTF J1901+1458 stood out because of the high-significance detection of its short period and its blue and faint location in the CMD (see Fig. 1).

Magnetic Field At low magnetic field strengths, the effect of magnetic field on hydrogen transitions can be calculated as a perturbation to the zero-field electron wavefunction. The perturbation lifts the degeneracy in the m quantum number, and each transition is split into three Zeeman components, corresponding to a change in m of $+1$, 0 and -1. In the strong regime (above ~ 100 MG), the magnetic and Coulomb terms are comparable, and the wavefunction does not have a spherical symmetry anymore. The perturbation method is not viable in this case, and the energies and oscil-

lator strengths of hydrogen transitions in this regime were calculated using variation methods[50–53]. An important characteristic of high-field transitions, is that some transitions become 'stationary', i.e. they go through a minimum or a maximum in energy and, at those fields strengths, appreciable changes in B only yield small changes in wavelength. The magnetic broadening at these transitions is considerably reduced, and therefore the absorption features are still detectable even after averaging the field over the surface of the white dwarf. We considered all the bound-bound transitions tabulated in Ruder et al. 1994[28] that follow selection rules, and we found that the features in the spectrum of ZTF J1901+1458 correspond to stationary lines in a ~ 800 MG field. The wavelengths of the transitions in this regime as a function of magnetic field strength are shown in the lower panels of Fig. 3. The identified features are numbered and the corresponding transitions are listed in Table 2, where the states are labelled by their asymptotic quantum numbers nlm for the zero-field states and by the numbers $NM\mu$ for $B \to \infty$, where μ defines the z parity of the states $[\pi = (-1)^{\mu}]$. A few lines show variations with phase (see Extended Data Fig 7 and 8), which can be attributed to the variation of the magnetic field strength across the surface. In particular, some of the features become narrower or broader depending on the phase, which indicates that the field is more or less uniform over the surface in different phases. Additionally, the feature at ~ 4600 Å(line 7) shifts in wavelength, going as low as ~ 4500 Å, which indicates that the magnetic field is as low as 600 MG on some regions on the surface of the white dwarf. This is also confirmed by the contamination of line 10 by line 11.

Photometric Fitting To determine the radius and effective temperature of ZTF J1901+1458, we made use of the Pan-STARRS[32] photometry already available to us, and the Gaia[17,49] parallax.

Table 2: Identified Balmer transitions. The numbers correspond to the identified transitions in Fig. 3 and the wavelengths of the transitions at 800 MG are from[28]. For 7 and 11, we also list the wavelength for 600 MG (left).

	line	$nlm \rightarrow n'l'm'$	$NM\mu \rightarrow N'M'\mu'$	λ [Å]
1	Balmer Hγ	$2s_0 \rightarrow 5p'_0$	$0\ 0\ 2 \rightarrow 0\ 0\ 11$	3344.23
2	Balmer Hγ	$2s_0 \rightarrow 5p'_{-1}$	$0\ 0\ 2 \rightarrow 0\ -1\ 10$	3370.41
3	Balmer Hγ	$2s_0 \rightarrow 5f'_0$	$0\ 0\ 2 \rightarrow 0\ 0\ 9$	3464.11
4	Balmer Hβ	$2s_0 \rightarrow 4p'_0$	$0\ 0\ 2 \rightarrow 0\ 0\ 7$	3694.56
5	Balmer Hβ	$2s_0 \rightarrow 4p'_{-1}$	$0\ 0\ 2 \rightarrow 0\ -1\ 6$	3805.82
6	Balmer Hβ	$2s_0 \rightarrow 4f'_0$	$0\ 0\ 2 \rightarrow 0\ 0\ 5$	4249.86
7	Balmer Hβ	$2s_0 \rightarrow 4f'_{-1}$	$0\ 0\ 2 \rightarrow 0\ -1\ 4$	4517.97, 4590.9
8	Balmer Hα	$2p_{-1} \rightarrow 3d_{-2}$	$0\ -1\ 0 \rightarrow 0\ -2\ 0$	5883.63
9	Balmer Hα	$2s_0 \rightarrow 3p_0$	$0\ 0\ 2 \rightarrow 0\ 0\ 3$	6615.06
10	Balmer Hα	$2p_0 \rightarrow 3d_{-1}$	$0\ 0\ 2 \rightarrow 0\ -1\ 1$	8525.69
11	Balmer Hα	$2s_0 \rightarrow 3p_{-1}$	$0\ 0\ 1 \rightarrow 0\ -1\ 2$	8537.76, 9542.62

In addition, we asked for Swift[31] UVOT[30] photometry (TOO proposal number 14380, target ID 13650). The photometric data used in the fitting is listed in Table 3. As the errors on the Pan-STARRS photometry is lower than the photometric variation, we used an error of 0.02 magnitudes instead to take into account the error induced by variability. We fitted the photometric data with the white dwarf 1D model DA (hydrogen dominated) atmospheres of Tremblay et al. 2011[54].

At the maximum surface gravity in the model grid ($\log g = 9.5$) and at the temperatures that we are considering here, the synthetic spectra present shallow Balmer absorption features (see Fig. 5, dashed black line). As the spectrum of ZTF J1901+1458 is almost featureless, instead of using the synthetic spectra directly in our fit, we employed eighth order polynomials fitted to the spectra to derive the synthetic photometry (e.g. the solid blue line in Fig. 5). In order to account for extinction, we applied reddening corrections to the synthetic spectra (and polynomials) using the Cardelli et al. 1989[55] extinction curves, available at `https://www.stsci.edu/`. From the corrected models, we computed synthetic photometry using the `pyphot` package (`https://mfouesneau.github.io/docs/pyphot/`).

In the fit, the free parameters were the effective temperature $T_{\rm eff}$ and radius R_* of the white dwarf, and the interstellar reddening $E(B-V)$. The best fit is shown in Fig. 5, while Fig. 6 illustrates the corner plots. In the fit, we assumed the nominal value of the Gaia parallax for the distance. As a change in distance would have the effect of changing the normalisation in the spectrum, the error on the distance only influences the error on the stellar radius, and therefore we included the error on the distance in the error on the radius. The errors quoted are the statistical errors derived from the Monte Carlo simulation shown in Fig. 6. They do not include possible

modelling errors due to the effect of magnetic field; however, as the photometric variation is quite small, we do not expect a the magnetic field to introduce a significant error on the synthetic values.

Theoretical Mass-Radius Relation In order to derive the mass of the white dwarf, we computed the mass-radius relation employing an equation-of-state that includes Coulomb corrections to the pressure and energy of a degenerate Fermi gas[56,57], as done in Hamada and Salpeter 1961[58] (H&S). Since ZTF J1901+1458 is so compact, general relativistic corrections are important and therefore, contrary to H&S, we did not integrate the Newtonian hydrostatic equilibrium equation, but rather the Tolman-Oppenheimer-Volkoff (TOV) equation[59,60]. Furthermore, we include thermal pressure which may be important in the outer layers of the star. The results are shown in Fig. 4 for several compositions. Our calculations were performed assuming either a thermal structure consistent with the luminosity of the white dwarf[39] or the zero-temperature limit. These yield essentially identical mass-radius relations because the temperature of the white dwarf is insufficient to change its structure significantly. For the composition of the carbon-burning ash, we use the results from Camisassa et al.[25]. For the density thresholds for the electron capture onto magnesium and neon[61], we use the values of 4×10^9 g cm^{-3} and 9×10^9 g cm^{-3} respectively. For sodium[41] we use 1.7×10^9 g cm^{-3}. We estimate the temperature at a density of 1.7×10^9 g cm^{-3} to be about 7×10^7 K; therefore, ZTF J1901+1458, unlike all other known white dwarfs, is cooling through the Urca process on ^{23}Na[40,41] which makes an age determination difficult. A preliminary simulation with MESA[62–66] confirmed the Urca processes as the main cooling processes in the core of the star. Using the 1.29 $M_\odot$ model of Camisassa et al.[25] yields an estimate of about 10 Myr which we take as a upper limit for the age of ZTF J1901+1458 because additional cooling processes are active.

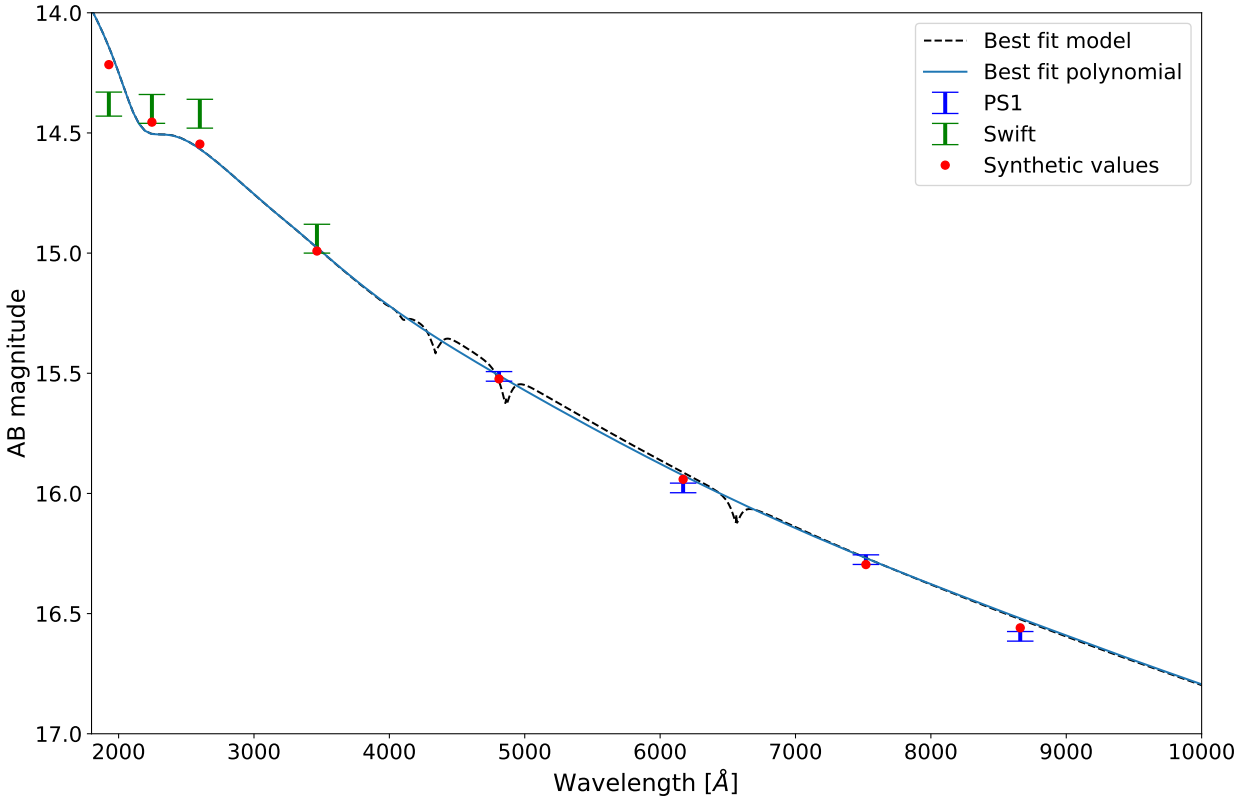

Figure 5: **Photometric fit.** The blue solid line shows the best-fitting polynomial, while the black dashed line shows the corresponding model spectrum, fitted to Pan-STARRS and Swift photometry to determine $T_{\rm eff}$, R_* and $E(B-V)$. The synthetic photometric values (obtained from the blue solid line) are shown in red, while the Swift values are shown in green with 1-σ error bars and the Pan-STARRS values in blue with the error that we chose to account for the photometric variability (0.02 mag).

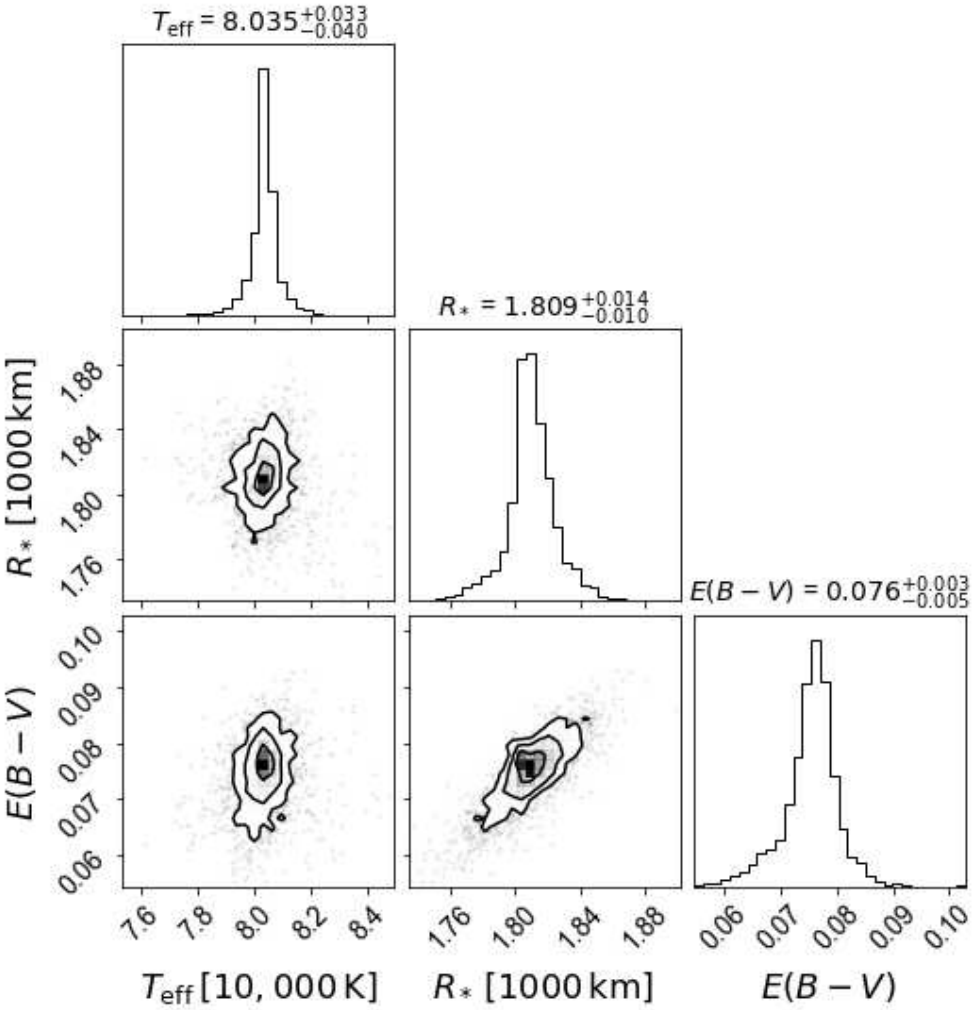

Figure 6: **Corner plots.** Corner plots for the photometric fitting. ZTF J1901+1458 is only at a distance of 41 pc and we therefore expect a low reddening. The reddening value is weakly correlated with the radius in the fitting, but a low reddening would only reduce the value of the radius.

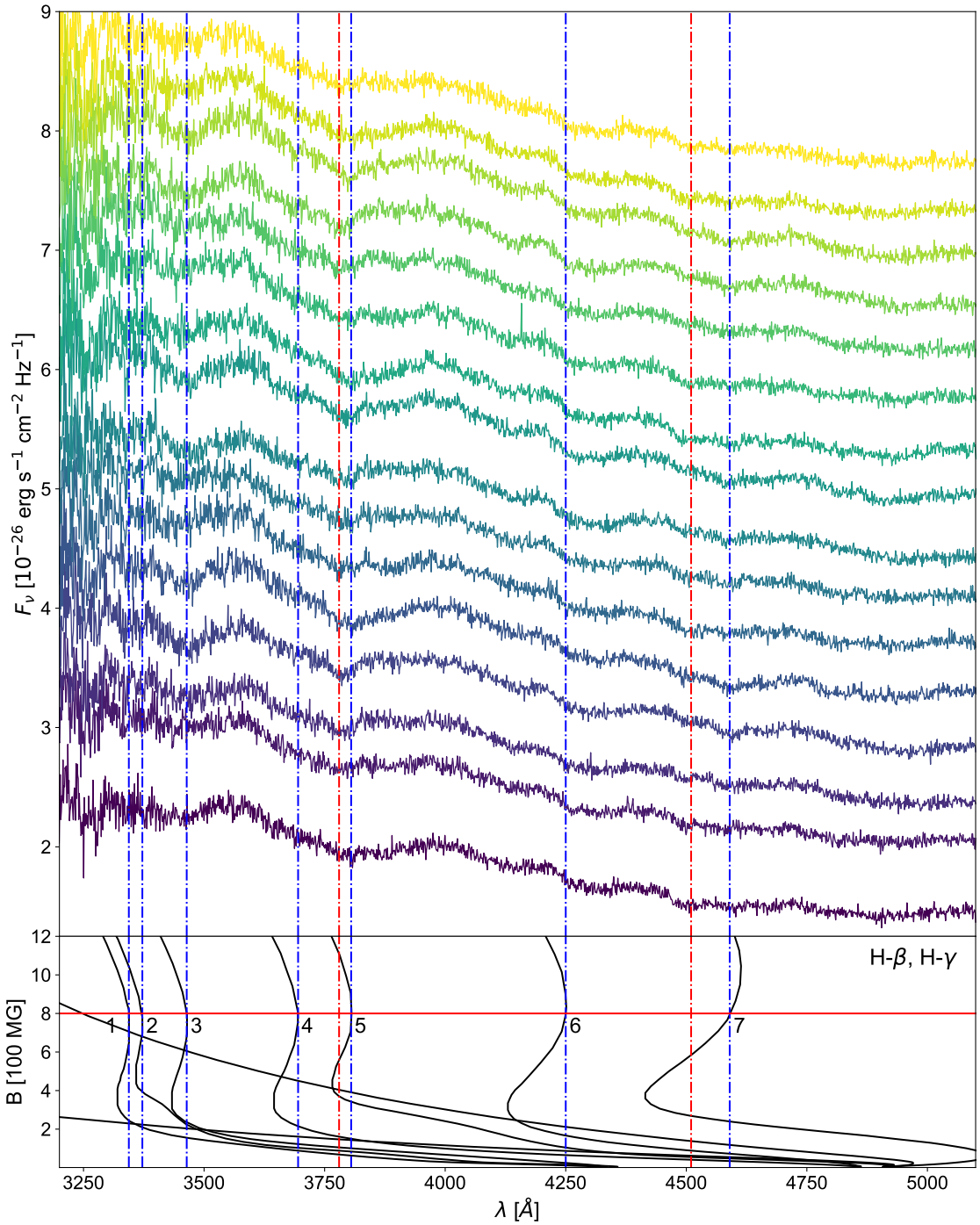

Figure 7: **Phase-resolved spectrum, blue side.** The LRIS phase-resolved spectrum of ZTF J1901+1458 in the blue side. Some small variations can be observed in the spectral features with phase, especially in features at ~ 4600 Å and at ~ 3800 Å.

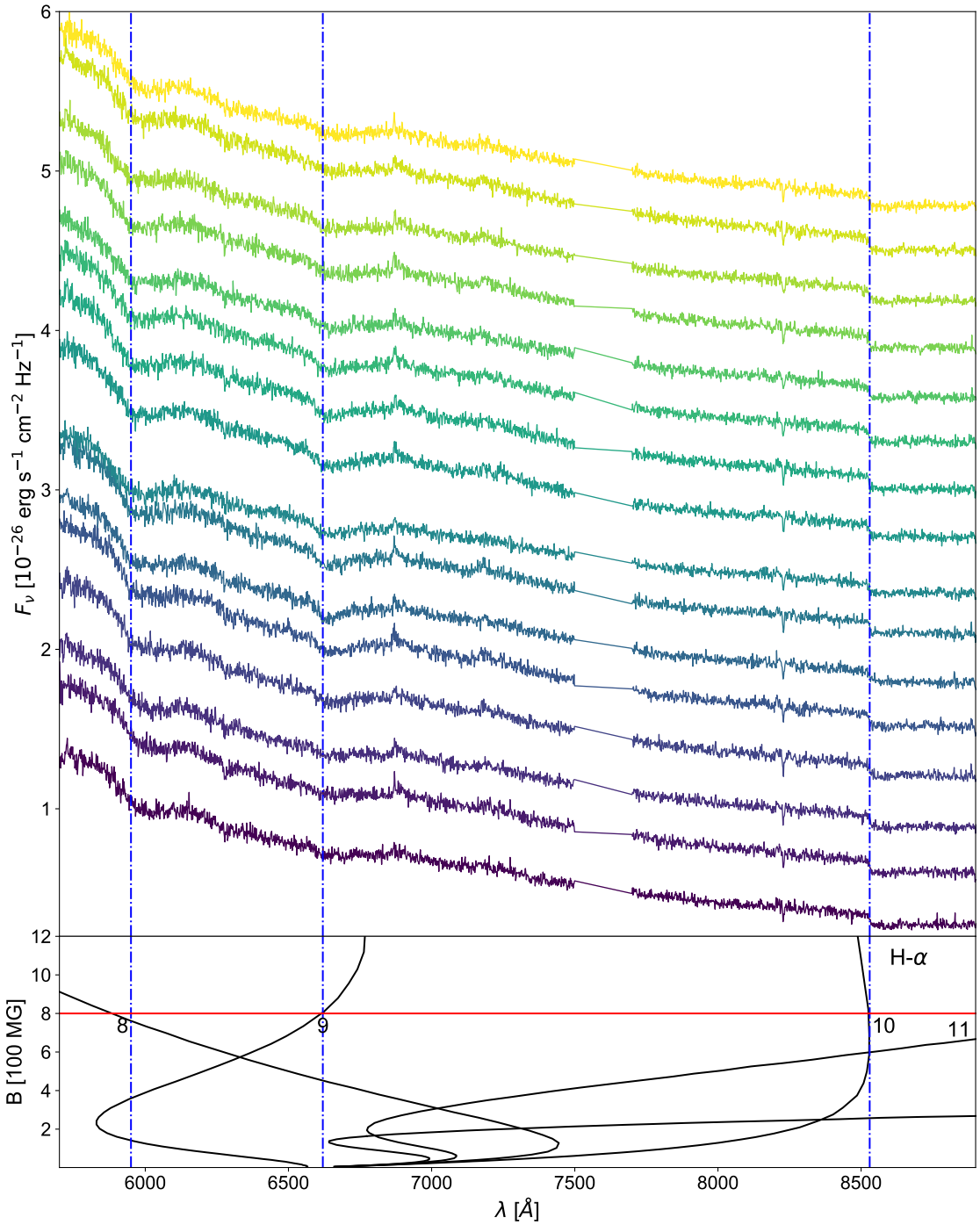

Figure 8: **Phase-resolved spectrum, red side.** The LRIS phase-resolved spectrum of ZTF J1901+1458 in the red side. Some small variations can be observed in the spectral features with phase, in particular the feature at ~ 6620 Å becomes broader and narrower with phase.

Table 3: Photometric data for ZTF J1901+1458.

PS1$-z$	PS1$-i$	PS1$-r$	PS1$-g$
16.595 ± 0.006	16.276 ± 0.003	15.977 ± 0.003	15.513 ± 0.002
UVOT$-U$	UVOT$-UVW1$	UVOT$-UVM2$	UVOT$-UVW2$
14.94 ± 0.06	14.42 ± 0.06	14.40 ± 0.06	14.38 ± 0.06

1. Brown, W. R. *et al.* The ELM Survey. VIII. Ninety-eight Double White Dwarf Binaries. *Astrophys. J.* **889**, 49 (2020). 2002.00064.

2. Burdge, K. B. *et al.* General relativistic orbital decay in a seven-minute-orbital-period eclipsing binary system. *Nat.* **571**, 528–531 (2019). 1907.11291.

3. Burdge, K. B. *et al.* A systematic search of Zwicky Transient Facility data for ultracompact binary LISA-detectable gravitational-wave sources. *arXiv e-prints* arXiv:2009.02567 (2020). 2009.02567.

4. Shen, K. J. Every Interacting Double White Dwarf Binary May Merge. *Astrophys. J. Lett.* **805**, L6 (2015). 1502.05052.

5. Dan, M., Rosswog, S., Brüggen, M. & Podsiadlowski, P. The structure and fate of white dwarf merger remnants. *Mon. Not. R. Astron. Soc.* **438**, 14–34 (2014). 1308.1667.

6. Tout, C. A. & et al. Binary star origin of high field magnetic white dwarfs. *Mon. Not. R. Astron. Soc.* **387**, 897–901 (2008). 0805.0115.

7. García-Berro, E. & et al. Double Degenerate Mergers as Progenitors of High-field Magnetic White Dwarfs. *Astrophys. J.* **749**, 25 (2012). 1202.0461.

8. Schwab, J. Evolutionary Models for the Remnant of the Merger of Two Carbon-Oxygen Core White Dwarfs (2020). (in press).

9. Reding, J. S. *et al.* An Isolated White Dwarf with 317 s Rotation and Magnetic Emission. *Astrophys. J.* **894**, 19 (2020). 2003.10450.

10. Pshirkov, M. S. *et al.* Discovery of a hot ultramassive rapidly rotating DBA white dwarf. *Mon. Not. R. Astron. Soc.* **499**, L21–L25 (2020). 2007.06514.

11. Ferrario, L., de Martino, D. & Gänsicke, B. T. Magnetic White Dwarfs. *Space Science Reviews* **191**, 111–169 (2015). 1504.08072.

12. Chandrasekhar, S. The Maximum Mass of Ideal White Dwarfs. *Astrophys. J.* **74**, 81 (1931).

13. Bellm, E. C. *et al.* The Zwicky Transient Facility: System Overview, Performance, and First Results. *Pub. Ast. Soc. Pac.* **131**, 018002 (2019). 1902.01932.

14. Graham, M. J. *et al.* The Zwicky Transient Facility: Science Objectives. *Pub. Ast. Soc. Pac.* **131**, 078001 (2019). 1902.01945.

15. Dekany, R. *et al.* The Zwicky Transient Facility: Observing System. *Pub. Ast. Soc. Pac.* **132**, 038001 (2020). 2008.04923.

16. Gentile Fusillo, N. P. & et al. A Gaia Data Release 2 catalogue of white dwarfs and a comparison with SDSS. *Mon. Not. R. Astron. Soc.* **482**, 4570–4591 (2019). 1807.03315.

17. Gaia Collaboration *et al.* The Gaia mission. *Astron. Astrophys.* **595**, A1 (2016). 1609.04153.

18. Harding, L. K. *et al.* CHIMERA: a wide-field, multi-colour, high-speed photometer at the prime focus of the Hale telescope. *Mon. Not. R. Astron. Soc.* **457**, 3036–3049 (2016). 1601.03104.

19. Berger, L., Koester, D., Napiwotzki, R., Reid, I. N. & Zuckerman, B. Rotation velocities of white dwarfs determined from the Ca II K line. *Astron. Astrophys.* **444**, 565–571 (2005). astro-ph/0509121.

20. Brinkworth, C. S. & et al. Measuring the Rotational Periods of Isolated Magnetic White Dwarfs. *Astrophys. J.* **773**, 47 (2013).

21. Hermes, J. J. & et al. White Dwarf Rotation as a Function of Mass and a Dichotomy of Mode Line Widths: Kepler Observations of 27 Pulsating DA White Dwarfs through K2 Campaign 8. *Astrophys. J. Supp.* **232**, 23 (2017). 1709.07004.

22. Kilic, M. *et al.* The 100 pc White Dwarf Sample in the SDSS Footprint. *Astrophys. J.* **898**, 84 (2020). 2006.00323.

23. Holberg, J. B. & Bergeron, P. Calibration of Synthetic Photometry Using DA White Dwarfs. *Astron. J.* **132**, 1221–1233 (2006).

24. Fontaine, G., Brassard, P. & Bergeron, P. The Potential of White Dwarf Cosmochronology. *Pub. Ast. Soc. Pac.* **113**, 409–435 (2001).

25. Camisassa, M. E. *et al.* The evolution of ultra-massive white dwarfs. *Astron. Astrophys.* **625**, A87 (2019). 1807.03894.

26. Van Grootel, V. *et al.* The instability strip of ZZ Ceti white dwarfs. I. Introduction of time-dependent convection. *Astron. Astrophys.* **539**, A87 (2012).

27. Oke, J. B. *et al.* The Keck Low-Resolution Imaging Spectrometer. *Pub. Ast. Soc. Pac.* **107**, 375 (1995).

28. Ruder, H., Wunner, G., Herold, H. & Geyer, F. *Atoms in Strong Magnetic Fields. Quantum Mechanical Treatment and Applications in Astrophysics and Quantum Chaos* (Springer, 1994).

29. Ferrario, L. & et al. EUVE J0317-855: a rapidly rotating, high-field magnetic white dwarf. *Mon. Not. R. Astron. Soc.* **292**, 205–217 (1997).

30. Roming, P. W. A. *et al.* The Swift Ultra-Violet/Optical Telescope. *Space Science Reviews* **120**, 95–142 (2005). astro-ph/0507413.

31. Gehrels, N. *et al.* The Swift Gamma-Ray Burst Mission. *Astrophys. J.* **611**, 1005–1020 (2004). astro-ph/0405233.

32. Chambers, K. C. *et al.* The Pan-STARRS1 Surveys. *arXiv e-prints* arXiv:1612.05560 (2016). 1612.05560.

33. Murai, T., Sugimoto, D., Hōshi, R. & Hayashi, C. Evolution of Carbon Stars. I —Gravitational Contraction and Onset of Carbon Burning—. *Progress of Theoretical Physics* **39**, 619–634 (1968).

34. Siess, L. Evolution of massive AGB stars. II. model properties at non-solar metallicity and the fate of Super-AGB stars. *Astron. Astrophys.* **476**, 893–909 (2007).

35. Nomoto, K. & Iben, J., I. Carbon ignition in a rapidly accreting degenerate dwarf - A clue to the nature of the merging process in close binaries. *Astrophys. J.* **297**, 531–537 (1985).

36. Kawai, Y., Saio, H. & Nomoto, K. Off-Center Ignition of Nuclear Burning in Merging White Dwarfs. *Astrophys. J.* **315**, 229 (1987).

37. Shen, K. J., Bildsten, L., Kasen, D. & Quataert, E. The Long-term Evolution of Double White Dwarf Mergers. *Astrophys. J.* **748**, 35 (2012). 1108.4036.

38. Külebi, B., Jordan, S., Nelan, E., Bastian, U. & Altmann, M. Constraints on the origin of the massive, hot, and rapidly rotating magnetic white dwarf RE J 0317-853 from an HST parallax measurement. *Astron. Astrophys.* **524**, A36 (2010). 1007.4978.

39. Hernquist, L. & Applegate, J. H. Analytical models of neutron star envelopes. *Astrophys. J.* **287**, 244–254 (1984).

40. Tsuruta, S. & Cameron, A. G. W. URCA Shells in Dense Stellar Interiors. *Astrophys. and Space Sc.* **7**, 374–406 (1970).

41. Schwab, J., Bildsten, L. & Quataert, E. The importance of Urca-process cooling in accreting ONe white dwarfs. *Mon. Not. R. Astron. Soc.* **472**, 3390–3406 (2017). 1708.07514.

42. Deloye, C. J. & Bildsten, L. Gravitational Settling of ^{22}Ne in Liquid White Dwarf Interiors: Cooling and Seismological Effects. *Astrophys. J.* **580**, 1077–1090 (2002). astro-ph/0207623.

43. Schwab, J., Quataert, E. & Bildsten, L. Thermal runaway during the evolution of ONeMg cores towards accretion-induced collapse. *Mon. Not. R. Astron. Soc.* **453**, 1910–1927 (2015). 1504.05194.

44. Leung, S.-C., Nomoto, K. & Suzuki, T. Electron-capture Supernovae of Super-AGB Stars: Sensitivity on Input Physics. *Astrophys. J.* **889**, 34 (2020). 1901.11438.

45. Diehl, R. *et al.* Radioactive ^{26}Al from massive stars in the Galaxy. *Nat.* **439**, 45–47 (2006). astro-ph/0601015.

46. Keane, E. F. & Kramer, M. On the birthrates of Galactic neutron stars. *Mon. Not. R. Astron. Soc.* **391**, 2009–2016 (2008). 0810.1512.

47. Burdge, K. B. *et al.* Orbital Decay in a 20 Minute Orbital Period Detached Binary with a Hydrogen-poor Low-mass White Dwarf. *Astrophys. J. Lett.* **886**, L12 (2019). 1910.11389.

48. Graham, M. J., Drake, A. J., Djorgovski, S. G., Mahabal, A. A. & Donalek, C. Using conditional entropy to identify periodicity. *Mon. Not. R. Astron. Soc.* **434**, 2629–2635 (2013). 1306.6664.

49. Gaia Collaboration *et al.* Gaia Data Release 2. Summary of the contents and survey properties. *Astron. Astrophys.* **616**, A1 (2018). 1804.09365.

50. Roesner, W., Wunner, G., Herold, H. & Ruder, H. Hydrogen atoms in arbitrary magnetic fields. I. Energy levels and wavefunctions. *Journal of Physics B Atomic Molecular Physics* **17**, 29–52 (1984).

51. Forster, H. *et al.* Hydrogen atoms in arbitrary magnetic fields. II. Bound-bound transitions. *Journal of Physics B Atomic Molecular Physics* **17**, 1301–1319 (1984).

52. Henry, R. J. W. & Oconnell, R. F. Hydrogen spectrum in magnetic white dwarfs : H alpha, H beta and H gamma transitions. *Pub. Ast. Soc. Pac.* **97**, 333–339 (1985).

53. Wunner, G., Roesner, W., Herold, H. & Ruder, H. Stationary hydrogen lines in white dwarf magnetic fields and the spectrum of the magnetic degenerate GRW +70 8247. *Astron. Astrophys.* **149**, 102–108 (1985).

54. Tremblay, P. E., Bergeron, P. & Gianninas, A. An Improved Spectroscopic Analysis of DA White Dwarfs from the Sloan Digital Sky Survey Data Release 4. *Astrophys. J.* **730**, 128 (2011). 1102.0056.

55. Cardelli, J. A., Clayton, G. C. & Mathis, J. S. The Relationship between Infrared, Optical, and Ultraviolet Extinction. *Astrophys. J.* **345**, 245 (1989).

56. Timmes, F. X. & Swesty, F. D. The Accuracy, Consistency, and Speed of an Electron-Positron Equation of State Based on Table Interpolation of the Helmholtz Free Energy. *Astrophys. J. Supp.* **126**, 501–516 (2000).

57. Schwab, J. python-helmholtz: Python bindings for Frank Timmes' Helmholtz EoS. (2020). URL https://doi.org/10.5281/zenodo.4056084.

58. Hamada, T. & Salpeter, E. E. Models for Zero-Temperature Stars. *Astrophys. J.* **134**, 683 (1961).

59. Tolman, R. C. Static Solutions of Einstein's Field Equations for Spheres of Fluid. *Physical Review* **55**, 364–373 (1939).

60. Oppenheimer, J. R. & Volkoff, G. M. On Massive Neutron Cores. *Physical Review* **55**, 374–381 (1939).

61. Miyaji, S., Nomoto, K., Yokoi, K. & Sugimoto, D. Supernova triggered by electron captures. *PASJ* **32**, 303–329 (1980).

62. Paxton, B. *et al.* Modules for Experiments in Stellar Astrophysics (MESA). *Astrophys. J. Supp.* **192**, 3 (2011). 1009.1622.

63. Paxton, B. *et al.* Modules for Experiments in Stellar Astrophysics (MESA): Planets, Oscillations, Rotation, and Massive Stars. *Astrophys. J. Supp.* **208**, 4 (2013). 1301.0319.

64. Paxton, B. *et al.* Modules for Experiments in Stellar Astrophysics (MESA): Binaries, Pulsations, and Explosions. *Astrophys. J. Supp.* **220**, 15 (2015). 1506.03146.

65. Paxton, B. *et al.* Modules for Experiments in Stellar Astrophysics (MESA): Convective Boundaries, Element Diffusion, and Massive Star Explosions. *Astrophys. J. Supp.* **234**, 34 (2018). 1710.08424.

66. Paxton, B. *et al.* Modules for Experiments in Stellar Astrophysics (MESA): Pulsating Variable Stars, Rotation, Convective Boundaries, and Energy Conservation. *Astrophys. J. Supp.* **243**, 10 (2019). 1903.01426.

67. Foreman-Mackey, D. corner.py: Scatterplot matrices in python. *The Journal of Open Source Software* **1**, 24 (2016). URL https://doi.org/10.21105/joss.00024.

68. Perley, D. A. Fully Automated Reduction of Longslit Spectroscopy with the Low Resolution Imaging Spectrometer at the Keck Observatory. *Pub. Ast. Soc. Pac.* **131**, 084503 (2019). 1903.07629.

Acknowledgements The authors would like to thank Shing-Chi Leung and Sterl Phinney for insightful discussions. I.C. thanks the Burke Institute at Caltech for supporting her research. J.F. is thankful for support through an Innovator Grant from The Rose Hills Foundation, and the Sloan Foundation through grant FG-2018-10515. K.B.B thanks the National Aeronautics and Space Administration and the Heising Simons Foundation for supporting his research. J.S. is supported by the A.F. Morrison Fellowship in Lick Observatory and by the National Science Foundation through grant ACI-1663688. This work was supported by the Natural Sciences and Engineering Research Council of Canada.

This work is based on observations obtained with the Samuel Oschin Telescope 48-inch and the 60-inch Telescope at the Palomar Observatory as part of the Zwicky Transient Facility project. ZTF is supported by the National Science Foundation under Grant No. AST-1440341 and a collaboration including Caltech, IPAC, the Weizmann Institute for Science, the Oskar Klein Center at Stockholm University, the University of Maryland, the University of Washington, Deutsches Elektronen-Synchrotron and Humboldt University, Los Alamos National Laboratories, the TANGO Consortium of Taiwan, the University of Wisconsin at Milwaukee, and Lawrence Berkeley National Laboratories. Operations are conducted by COO, IPAC, and UW.

Some of the data presented herein were obtained at the W.M. Keck Observatory, which is operated as a scientific partnership among the California Institute of Technology, the University of California and the National Aeronautics and Space Administration.

This work has made use of data from the European Space Agency (ESA) mission *Gaia* (https://www.cosmos.esa.int/gaia), processed by the *Gaia* Data Processing and Analysis Consortium (DPAC, https://www.cosmos.esa.int/web/gaia/dpac/consortium). Funding for the DPAC has been provided by national institutions, in particular the institutions participating in the *Gaia* Multilateral Agreement.

The Pan-STARRS1 Surveys (PS1) and the PS1 public science archive have been made possible through contributions by the Institute for Astronomy, the University of Hawaii, the Pan-STARRS Project Office, the Max-Planck Society and its participating institutes, the Max Planck Institute for Astronomy, Heidelberg and the Max Planck Institute for Extraterrestrial Physics, Garching, The Johns Hopkins University, Durham University, the University of Edinburgh, the Queen's University Belfast, the Harvard-Smithsonian Center for Astrophysics, the Las Cumbres Observatory Global Telescope Network Incorporated, the National Central University of Taiwan, the Space Telescope Science Institute, the National Aeronautics and Space Administration under Grant No. NNX08AR22G issued through the Planetary Science Division of the NASA Science Mission Directorate, the National Science Foundation Grant No. AST-1238877, the University of Maryland, Eotvos Lorand University (ELTE), the Los Alamos National Laboratory, and the Gordon and Betty Moore Foundation.

We used the `pyphot` package (`https://mfouesneau.github.io/docs/pyphot/`) and the `corner.py` package[67].

The LRIS spectra were reduced using the `Lpipe` pipeline[68].

Author Contributions I.C. reduced the UV data, conducted the spectral and photometric analysis, identified the magnetic field and is the primary author of the manuscript. K.B.B. performed the period search on ZTF data and reduced the optical data. I.C. and J.H. conducted the mass-radius analysis. I.C., K.B.B., J.F.,

J.H., S.R.K., T.A.P., H.R. and J.S. contributed to the physical interpretation of the object. J.S. constructed preliminary MESA models for the object. I.A., A.D., D.A.D., A.A.M., F.J.M., R.S. and M.T.S. contributed to the implementation of ZTF. G.H. is a co-PI of ZTF MSIP. T.A.P. is the co-PI and S.R.K. is the PI of ZTF.

Data Availability Upon request, I.C. will provide the reduced photometric and spectroscopic data, and available ZTF data for the object. The astrometric and photometric data are already in the public domain, and they are readily accessible in the Gaia, Pan-STARSS catalogues and in the Swift database.

Code availability Upon request, I.C. will provide the code used to analyse the spectroscopic and photometric data. The code is written in Python.

Competing Interests The authors declare that they have no competing financial interests.

Correspondence Correspondence and requests for materials should be addressed to I.C. (email: ilariac@caltech.edu).

Figures

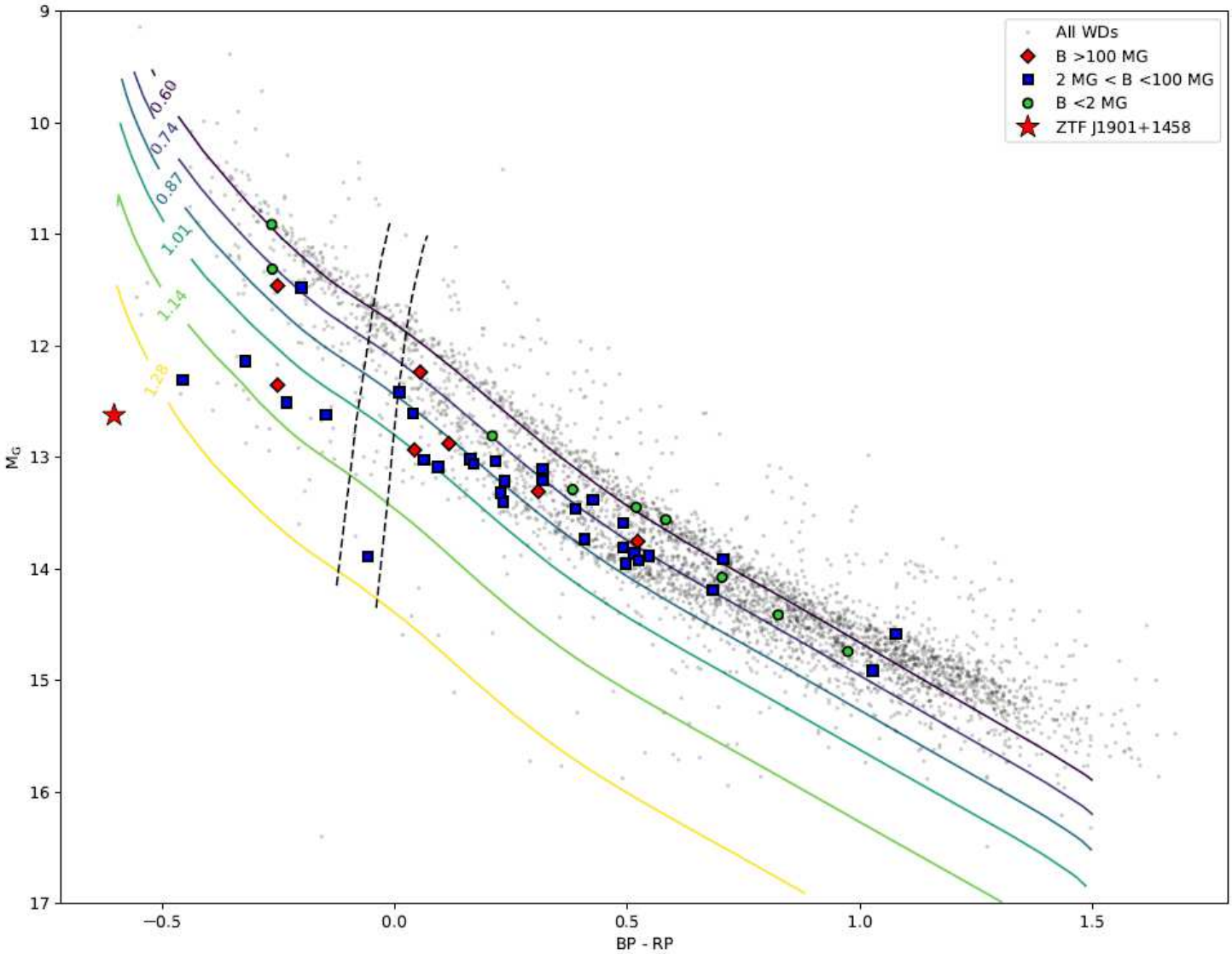

Figure 1

Gaia CMD. Gaia color-magnitude diagram for the white dwarfs that are within 100 pc from Earth and within the SDSS footprint22. Solid lines show theoretical cooling tracks for white dwarfs with masses between 0.6 M⊠ (top) and 1.28 Mo (bottom), equally spaced in mass; the atmosphere is assumed to be hydrogen-dominated23 and the interior composition to be carbon-oxygen24 for M < 1.1 Mo and oxygen-neon25 for M > 1.1 Mo. Coloured markers indicate white dwarfs for which a magnetic field was measured11. ZTF J1901+1458 is shown as a red star, and its location in the CMD reveals its high mass. Vertical dashed lines indicate the location of the ZZ-Ceti instability strip26. While ZTF J1901+1458's period is consistent with what is expected for non-radial pulsations, its temperature places it far away from the instability strip. Reddening corrections were applied only to ZTF J1901+1458; as the objects in the sample are close, reddening is expected to be small.

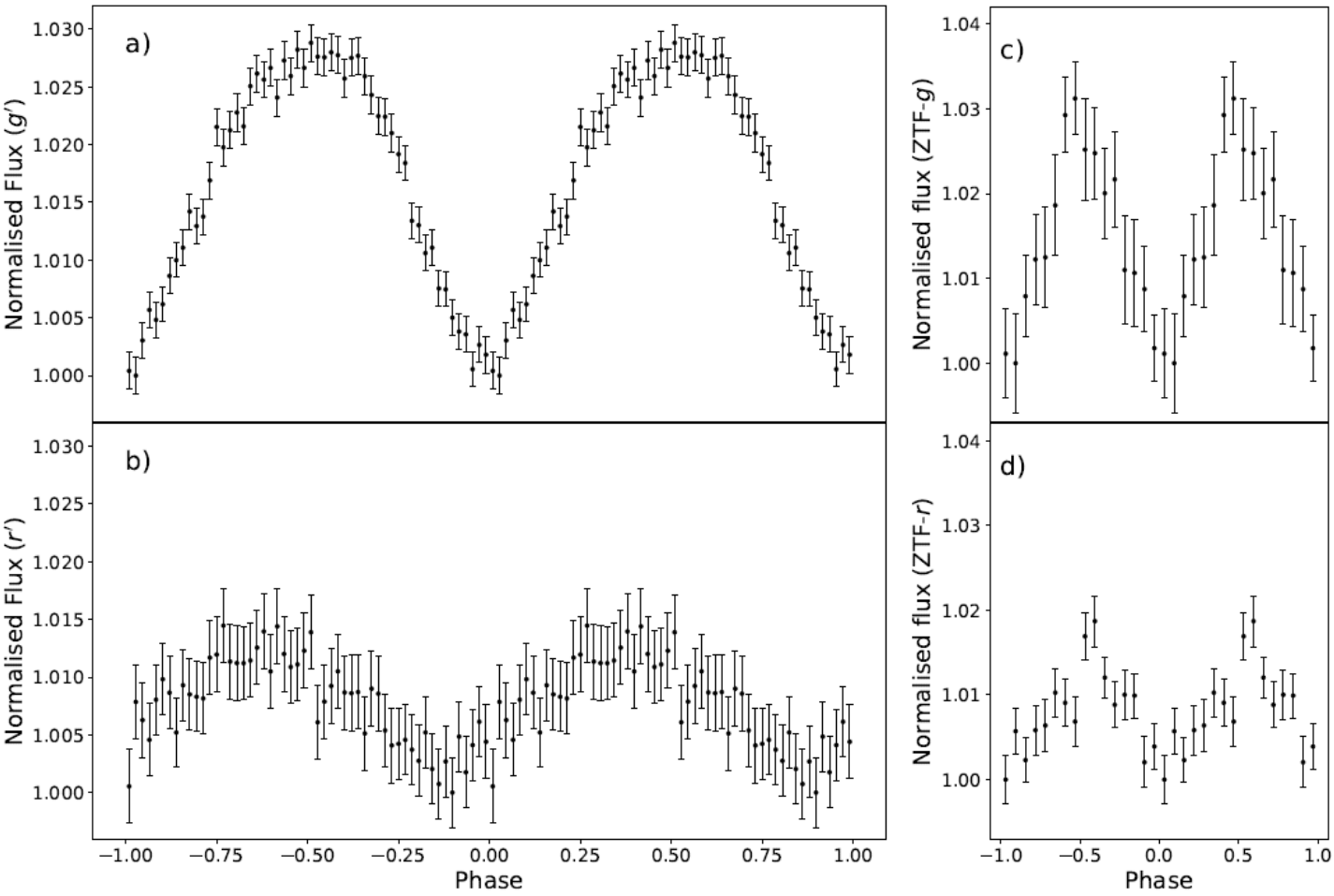

Figure 2

ZTF J1901+1458 lightcurve The left panels show the binned CHIMERA lightcurve phase-folded at a period of 6.94 minutes in the g'-band (a) and in the r'-band (b). The flux has been normalised to the minimum of the lightcurve in each band. The amplitude of the photometric variation is higher in the g'-band (about 3% peak-to-peak) than in the r'-band (∼ 1.5%). Addi-tionally, the two filters show a difference in phase: the red lags the green by about 51 s. The right panels show the similarly normalised ZTF discovery lightcurve in the ZTF g-band (c) and r−band (d). The error bars indicate 1-σ errors.

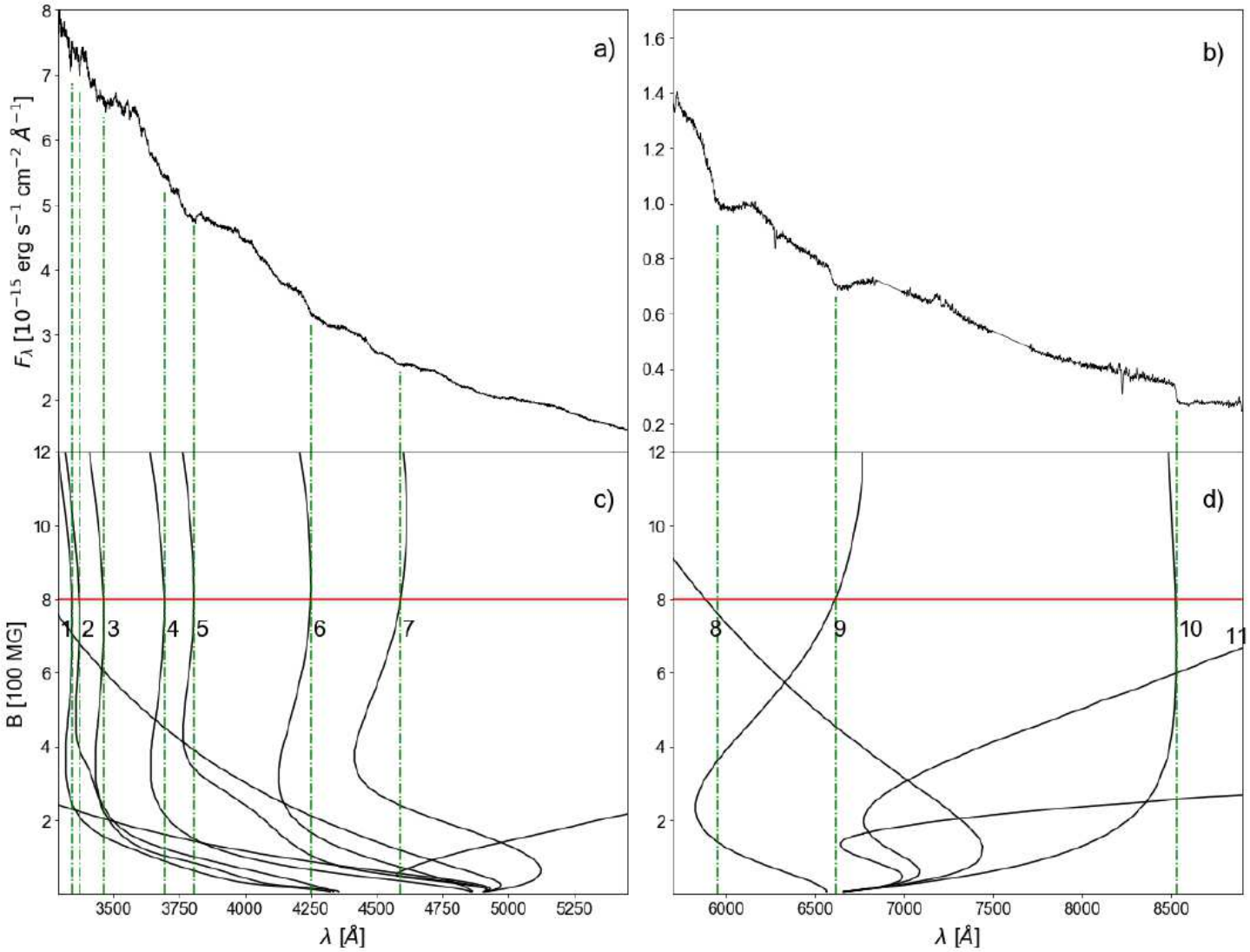

Figure 3

ZTF J1901+1458 optical spectrum. The LRIS phase-averaged spectrum of ZTF J1901+1458 is shown in black in the upper panels for the blue (a) and red (b) sections. In (c)-(d) the spectrum is compared to predicted line positions of Hα, Hβ and Hγ as a function of magnetic field28, showing that the white dwarf is characterised by a field strength of about 800 MG (red horizontal solid line). The identified absorption features are highlighted by the green dash-and-dotted lines and numbered, and the respective transitions are listed in Extended Data Table 2.

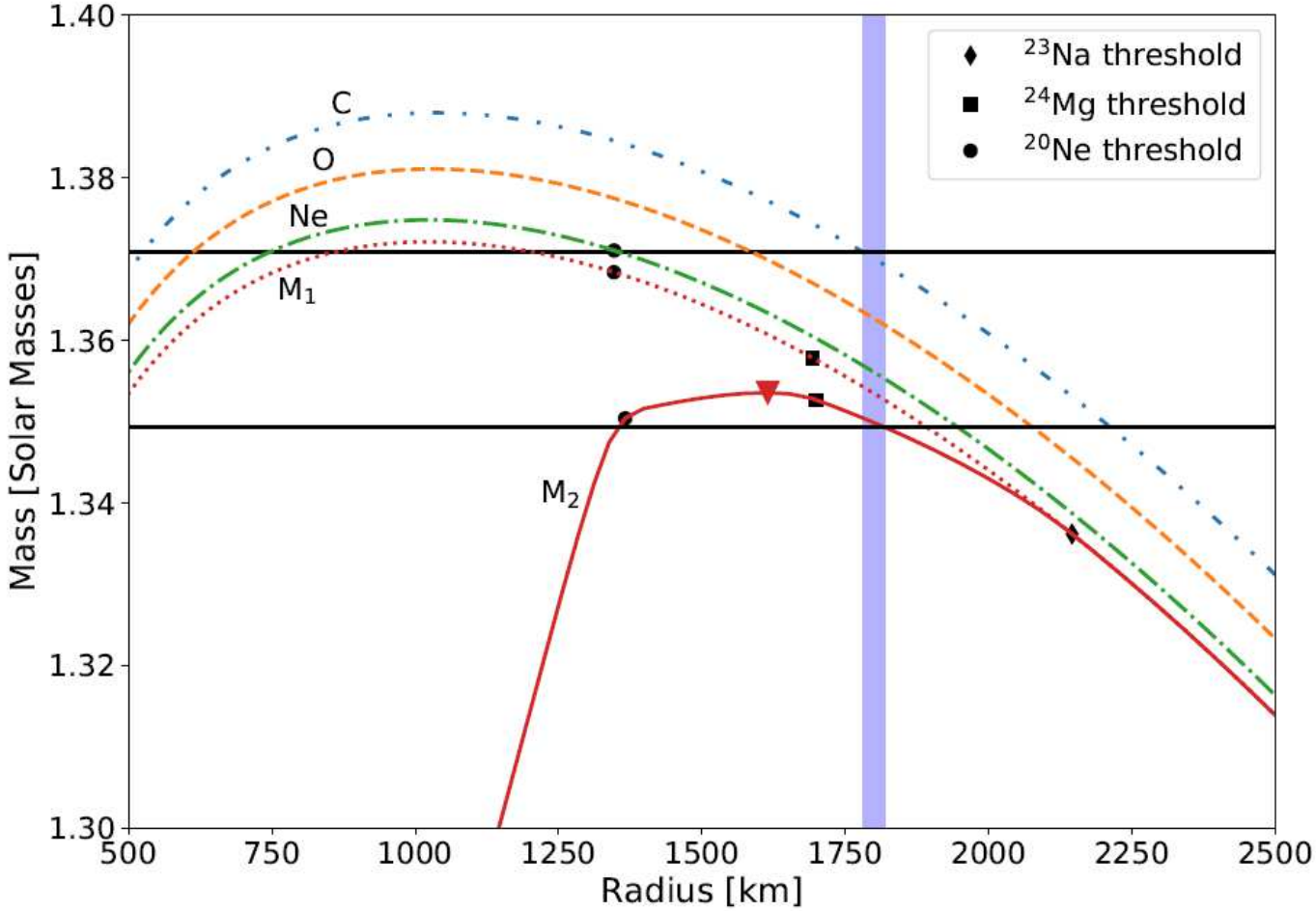

Figure 4

Mass-radius relation. The white dwarf mass-radius relation at the temperature of ZTF J1901+1458 (80,000 K) is shown for different compositions neglecting the effect of elec-tron captures: carbon C; oxygen O; neon Ne; and the mixture that is thought to result from carbon burning (M1), specifically 58% oxygen, 30% neon, 2% carbon, 5% sodium, and 5% magnesium25. The lowermost red solid curve (M2) traces the result from the carbon-burning-ash mixture includ-ing the effect of electron captures (see text). The black dots along each track indicate the central density threshold for inverse beta-decay of neon (circle), magnesium (square) and sodium (dia-mond). The vertical blue-shaded area indicates the observed radius of ZTF J1901+1458 within 1-σ errors. A red triangle indicates the maximum mass of 1.354 M at a radius of 1,600 km along the track of the mixed composition. The horizontal black solid lines highlight the mass determined using a radius of 1798 km for the upper line (pure C), 1.371 Mo and of 1824 km for the lower line (carbon-burning-ash mixture), 1.350 M0.

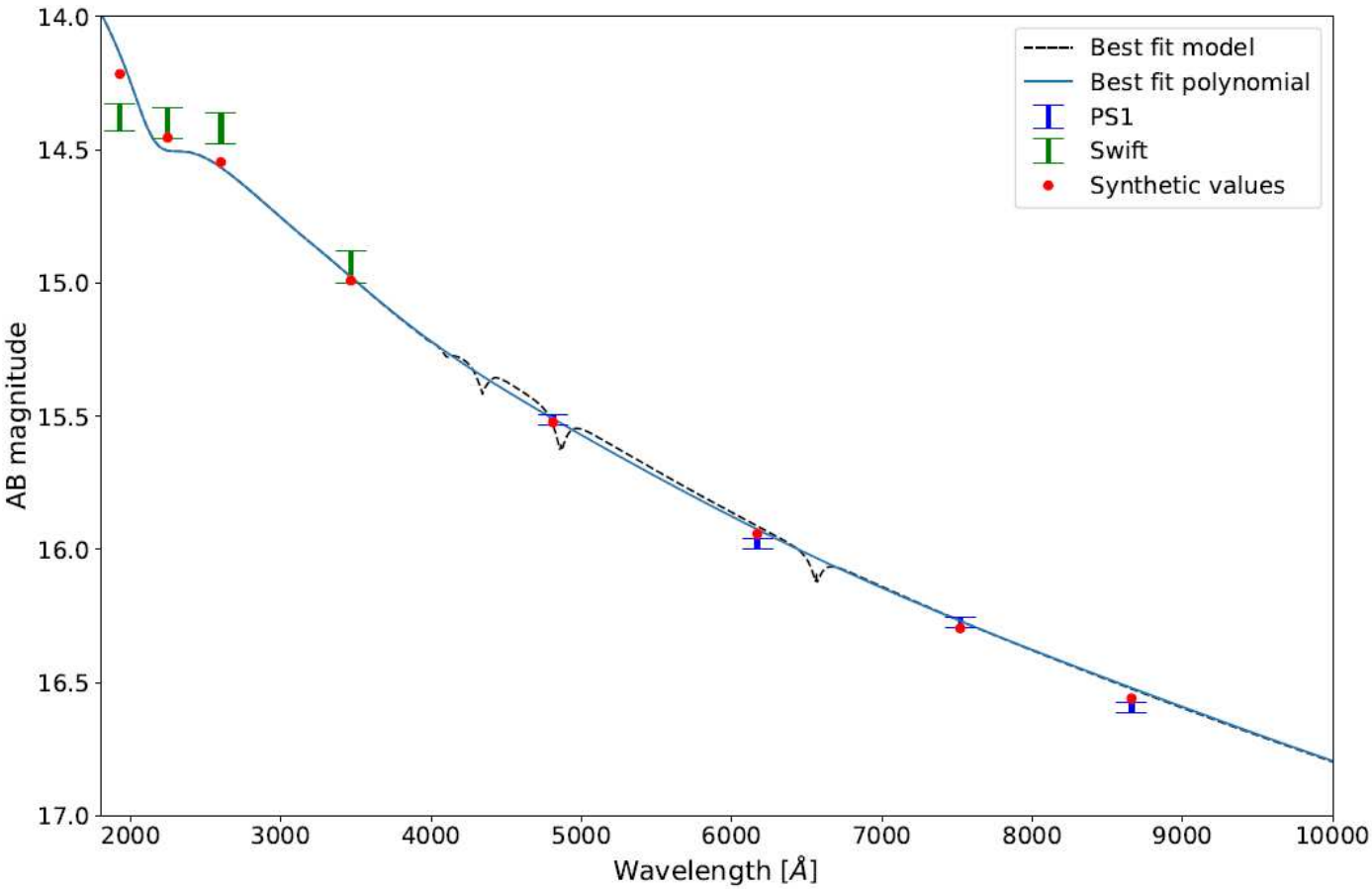

Figure 5

Photometric fit. The blue solid line shows the best-fitting polynomial, while the black dashed line shows the corresponding model spectrum, fitted to Pan-STARRS and Swift photometry to determine Teff , R and E(B − V). The synthetic photometric values (obtained from the blue solid line) are shown in red, while the Swift values are shown in green with 1-σ error bars and the Pan-STARRS values in blue with the error that we chose to account for the photometric variability (0.02 mag).

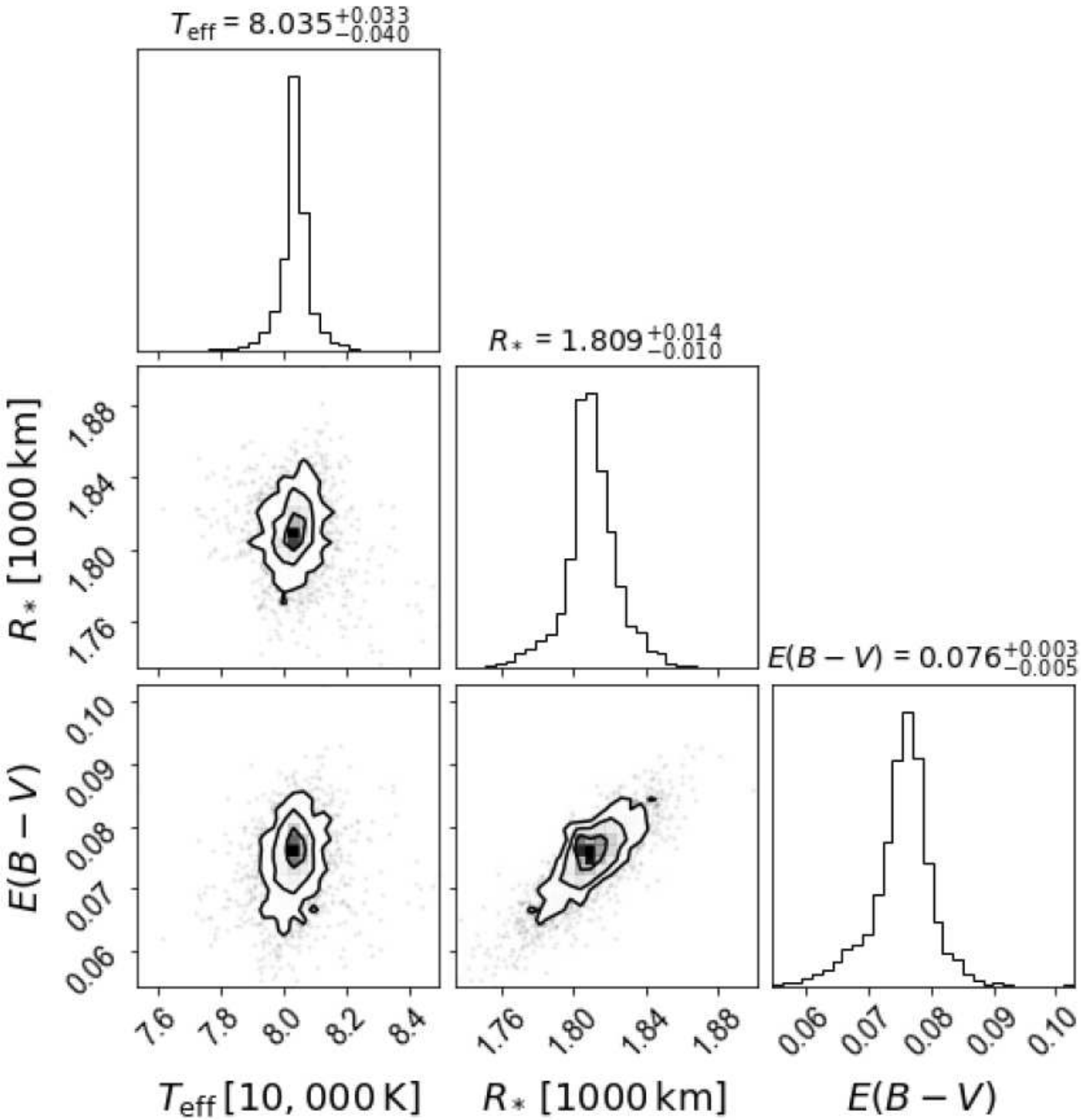

Figure 6

Corner plots. Corner plots for the photometric fitting. ZTF J1901+1458 is only at a distance of 41 pc and we therefore expect a low reddening. The reddening value is weakly correlated with the radius in the fitting, but a low reddening would only reduce the value of the radius.

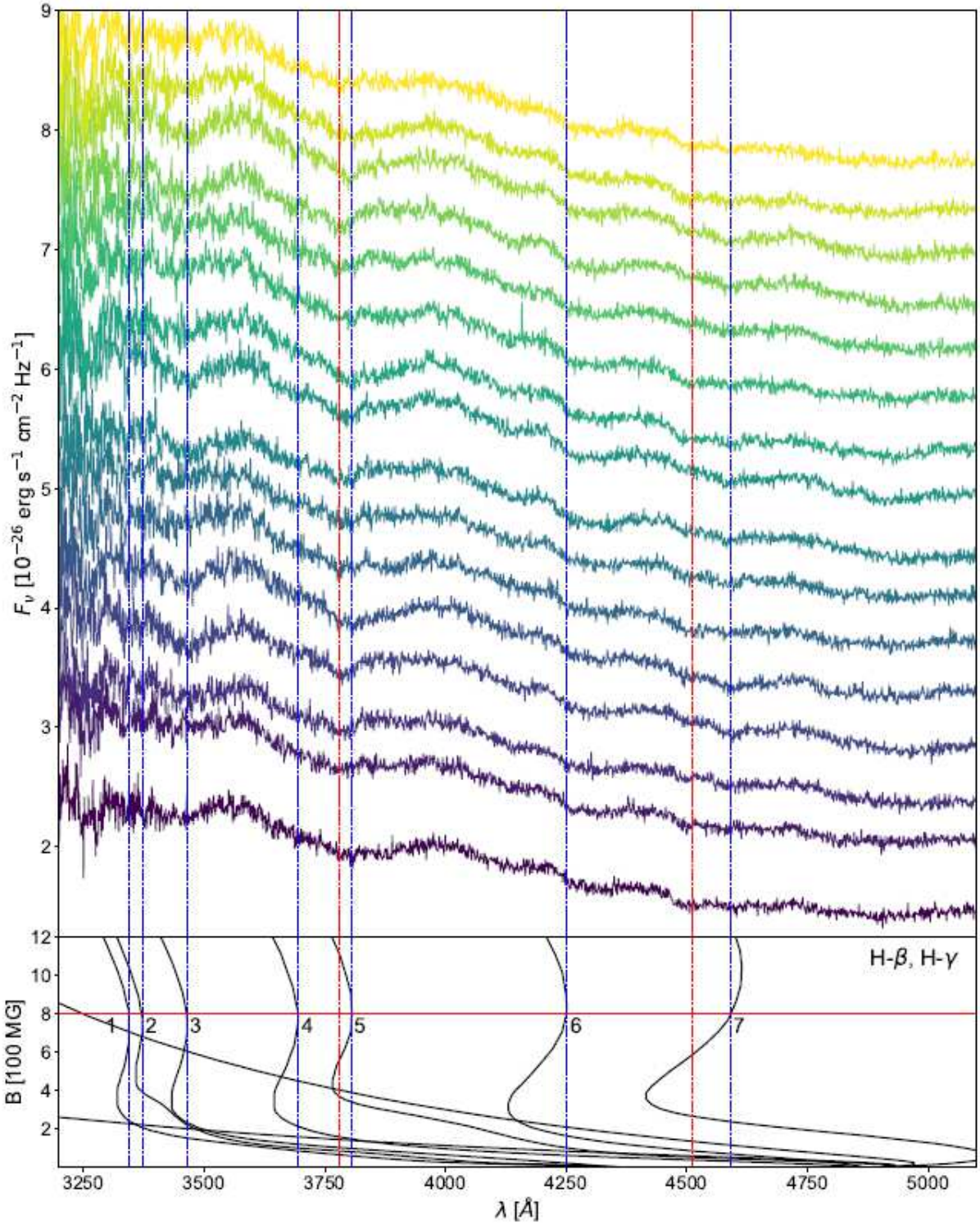

Figure 7

Phase-resolved spectrum, blue side. The LRIS phase-resolved spectrum of ZTF J1901+1458 in the blue side. Some small variations can be observed in the spectral features with phase, especially in features at ≈ 4600 °A and at ≈ 3800 °A.

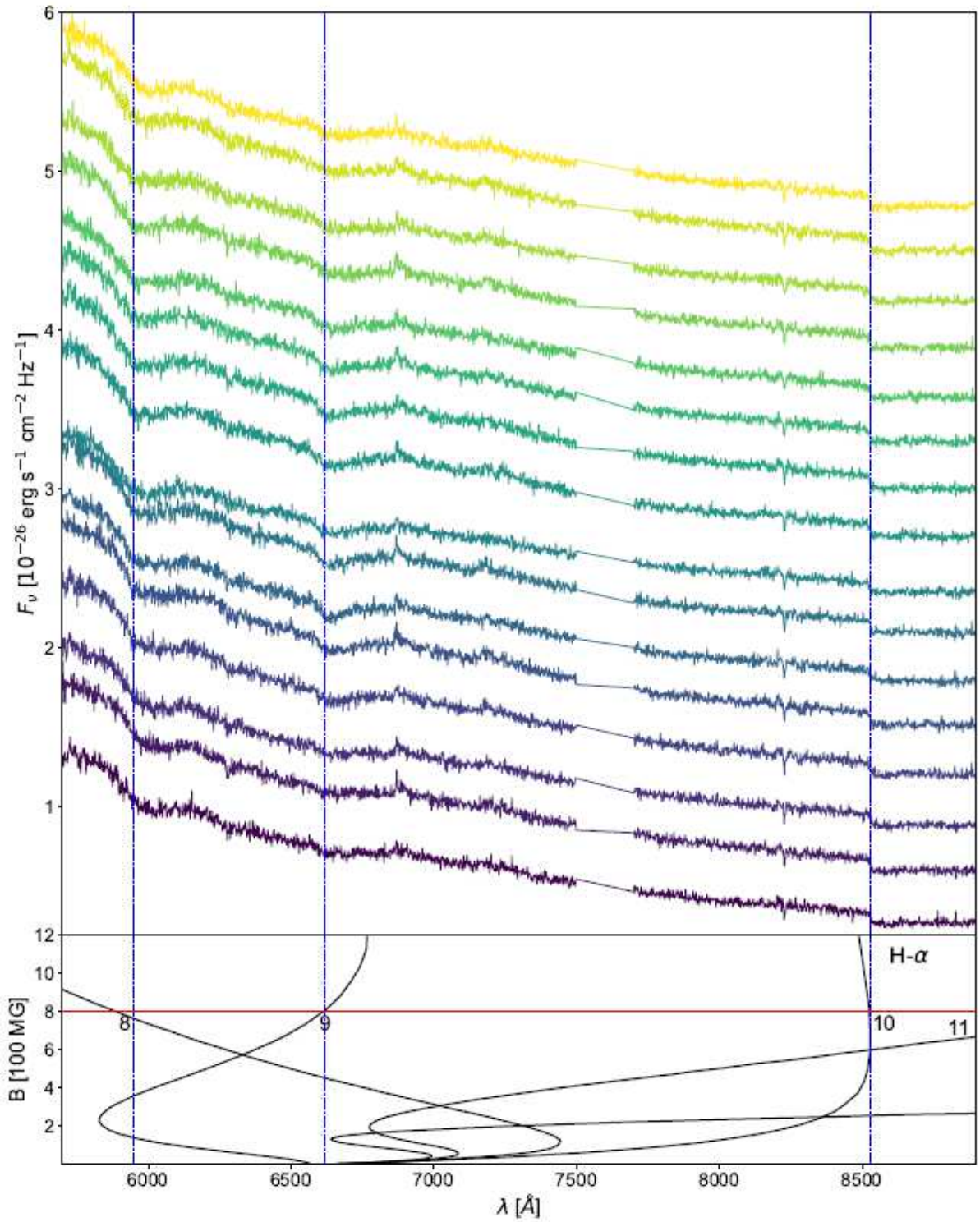

Figure 8

Phase-resolved spectrum, red side. The LRIS phase-resolved spectrum of ZTF J1901+1458 in the red side. Some small variations can be observed in the spectral features with phase, in particular the feature at ⊠ 6620 °A becomes broader and narrower with phase.